

Article

# Disturbance Rejection Control Method for Isolated Three-Port Converter with Virtual Damping

Jiang You <sup>1</sup>, Mengyan Liao <sup>1</sup>, Hailong Chen <sup>2,\*</sup>, Negareh Ghasemi <sup>3</sup> and Mahinda Vilathgamuwa <sup>4</sup>

<sup>1</sup> College of Automation, Harbin Engineering University, Harbin 150001, China; youjiang@hrbeu.edu.cn (J.Y.); liaomengyan417@163.com (M.L.)

<sup>2</sup> College of Shipbuilding Engineering, Harbin Engineering University, Harbin 150001, China

<sup>3</sup> School of Information Technology and Electrical Engineering, The University of Queensland, Brisbane 4072, Australia; n.ghasemi@uq.edu.au

<sup>4</sup> School of Electrical Engineering and Computer Science, Queensland University of Technology, Brisbane 4000, Australia; mahinda.vilathgamuwa@qut.edu.au

\* Correspondence: chen hailong@hrbeu.edu.cn; Tel.: +86-137-9665-8929

Received: 19 October 2018; Accepted: 13 November 2018; Published: 18 November 2018



**Abstract:** The high-power density and capability of three-port converters (TPCs) in generating demanded power synchronously using flexible control strategy make them potential candidates for renewable energy applications to enhance efficiency and power density. The control performance of isolated TPCs can be degraded due to the coupling and interaction of power transmission among different ports, variations of model parameters caused by the changes of the operation point and resonant peak of LC circuit. To address these issues, a linear active disturbance rejection control (LADRC) system is developed in this paper for controlling the utilized TPC. A virtual damping based method is proposed to increase damping ratio of current control subsystem of TPC which is beneficial in further improving dynamic control performance. The simulation and experimental results show that compared to the traditional frequency control strategy, the control performance of isolated TPC can be improved by using the proposed method.

**Keywords:** three-port converter; linear active disturbance rejection control; virtual damping; linear extended state observer

## 1. Introduction

The demand for three-port converters (TPCs) in renewable energy generation systems is increasing due to the compact structure of these converters and their ability to handle demanded power synchronously [1–5]. The TPCs not only facilitate multifunctional and multidirectional regulation for electrical power transmission but also provide flexibility in power control and power density enhancement in power conversion systems [6–10].

In an isolated three-port converter, the three windings of an isolated transformer share the same magnetic core, therefore there are unavoidable couplings of power transmission among the three ports of TPC. Decoupling control methods with proper decoupling factors are usually employed in three-port converters to achieve two single-input single-output (SISO) subsystems [11–14]. A classical frequency control theory is usually utilized to design controllers for each port respectively. Since the small signal models employed to design the controllers are produced by linearization of the nonlinear model of TPC at a steady-state operating point, the decoupling and dynamic performances of TPC control system can be degraded significantly by the variation of the operating point. Particularly, since the small signal models of TPC depend on a specific operating point, in a transient state process, a heavy change of the operating point parameters may affect decoupling of different ports and

dynamic performance of the control system. Generally, the three-port converter is a multiple-input multiple-output (MIMO) system, several phase-shifting angles and equivalent duty cycles can be used as control signals, and several voltages and currents of different ports can be assigned as the output signals. A linear quadratic regulator (LQR) based method is applied in ref. [15] to develop a multivariable controller for a three-port converter. Though the LQR method seems capable of achieving performance balance of different ports, it has relatively high sensitivity to the accuracy of system parameters. The parameters of the control models will vary with the change in operating point as these small signal based models used in the control system design are derived at a specific steady state operating point. Also, the design of the parameters of the time domain based LQR method is relatively complex compared to the frequency domain design method.

The LADRC method was first proposed by Zhiqiang Gao, and it has advantages of tolerating changes in model parameters and possesses an inherent decoupling ability that is useful for control system design [16]. In the LADRC method, the influences of model parameter deviations and external interferences can all be regarded as a generalized disturbance [17]. Therefore, the linear extended state observer (LESO) [18,19] can be used to estimate the state variables and generalized disturbance, and the observed signals are used to synthesize control signal in the control system. Compared to conventional PI controller, the LADRC method is shown to enhance the dynamic performance of the control system in [20].

In order to improve the dynamic control performance of an isolated three-port converter in this study, the LADRC method is employed to decrease negative impact of reactions among different ports, and obtain high control performance under load change conditions.

The rest of the paper is organized as follows. In Section 2, the topology, modulation method, power delivery relationship, and control-oriented small signal models are presented. The design of a LADRC based control system for a three-port converter by utilizing its current and voltage control small signal models, and the proposed virtual damping method to suppress the resonant peak in the current control subsystem are given in Section 3. Also, in this section, the principle and the design procedure of decoupling control are briefly illustrated for comparison purposes. The simulation and experiment results are presented in Section 4. Finally, the conclusion is provided in Section 5.

## 2. Topology and Modeling of TPC

The circuit topology of an isolated TPC is presented in Figure 1a. In this figure, a DC power supply (e.g., it can be a fuel cell or a photovoltaic cell) is set in Port 1, and the power supply,  $v_{d1}$  is connected in series with an inductor  $L_{d1}$ , and  $r_e$  represents the equivalent series resistance (ESR) of  $L_{d1}$ . There is  $180^\circ$  phase shift between leg A and leg B, and the duty cycles of all switches in Port 1 are set to be 50% and the drive signals of the switches on the same leg are complementary. The Port 2 and Port 3 are connected with load and energy storage (ES) respectively and their switching patterns are as same as the switching mode of Port 1. A simplified equivalent  $\Delta$ -connected circuit of the TPC by transferring the related parameters of Port 2 and Port 3 to Port 1 is given in Figure 1b. If the voltage between the middle points of leg A and leg B,  $v_1$  is defined as a reference, the phase shifts of  $v_2$  and  $v_3$  relative to  $v_1$  are denoted as  $\varphi_{12}$  and  $\varphi_{13}$  respectively, and they are shown in Figure 1c. Moreover,  $L_1$ ,  $L_2$ , and  $L_3$  are equivalent series inductances (including winding leakage inductance and additional inductance) of the three transformer windings. The expressions of  $L_{12}$ ,  $L_{13}$ , and  $L_{23}$  of the  $\Delta$ -connected circuit shown in Figure 1b are defined by (1).

$$\begin{cases} L_{12} = L_1 + L_2' + L_1 L_2' / L_3' \\ L_{23} = L_2' + L_3' + L_2' L_3' / L_1 \\ L_{13} = L_3' + L_1 + L_1 L_3' / L_2' \end{cases} \quad (1)$$

$L'_2$  and  $L'_3$  are expressed by (2).

$$L'_2 = \frac{N_1^2 L_2}{N_2^2}, L'_3 = \frac{N_1^2 L_3}{N_3^2} \quad (2)$$

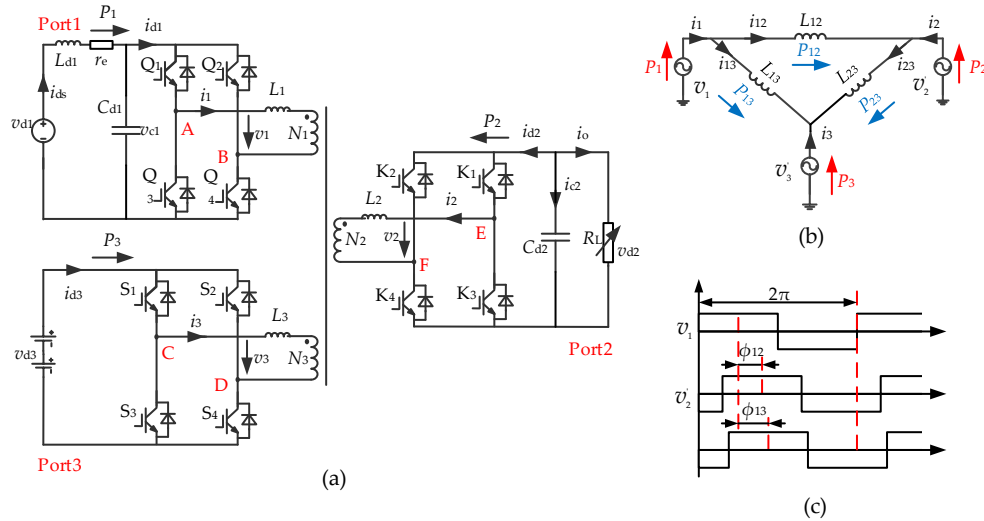


**Figure 1.** The isolated three-port converter: (a) topology; (b) equivalent  $\Delta$ -connected circuit; (c) modulation scheme.

In each switching cycle, the total power transmitted between any two ports is approximated to its fundamental component. Therefore, the Fourier expansion based fundamental component analysis method is employed for theoretical analysis in this study. By utilizing the equivalent  $\Delta$ -connection circuit in Figure 1b, the power equations of each port can be written as in (3).

$$\begin{cases} P_1 = P_{12} + P_{13} \\ P_2 = -P_{12} + P_{23} \\ P_3 = -P_{13} - P_{23} \end{cases}, (P_1 + P_2 + P_3 = 0) \quad (3)$$

where

$$\begin{cases} P_{12} = \frac{8N_1}{\pi^2 N_2 \omega_s L_{12}} V_{d1} V_{d2} \sin \varphi_{12} \\ P_{13} = \frac{8N_1}{\pi^2 N_3 \omega_s L_{13}} V_{d1} V_{d3} \sin \varphi_{13} \\ P_{23} = \frac{8N_1^2}{\pi^2 N_2 N_3 \omega_s L_{23}} V_{d2} V_{d3} \sin(\varphi_{13} - \varphi_{12}) \end{cases} \quad (4)$$

In (4),  $V_{d1}$ ,  $V_{d2}$ , and  $V_{d3}$  are the rated amplitudes of  $v_1$ ,  $v_2$ , and  $v_3$ ,  $N_1$ ,  $N_2$ , and  $N_3$  are the transformer winding turns of respective ports, and  $\omega_s$  is the switching angular frequency. Since the summation of  $P_1$ ,  $P_2$  and  $P_3$  is kept at zero as shown in (3), that means the power of one port can be determined using the powers of the other two ports. From this point of view, the energy storage port is usually taken as an energy buffer that can be charged or discharged determined by the power delivery and load conditions of Port 1 and Port 2 respectively. According to (3) and (4), the power of Port 1 and Port 2 can be formulated as (5) and (6) respectively.

$$P_1 = \frac{8N_1 V_{d1} V_{d2}}{\pi^2 N_2 \omega_s L_{12}} \sin \varphi_{12} + P_1 = \frac{8N_1 V_{d1} V_{d3}}{\pi^2 N_3 \omega_s L_{13}} \sin \varphi_{13} \quad (5)$$

$$P_2 = -\frac{8N_1 V_{d1} V_{d2} \sin \varphi_{12}}{\pi^2 N_2 \omega_s L_{12}} + \frac{8N_1 V_{d2} V_{d3} \sin(\varphi_{13} - \varphi_{12})}{\pi^2 N_2 N_3 \omega_s L_{23}} \quad (6)$$

Therefore, the corresponding average currents in each switching cycle can be derived as (7) and (8) respectively.

$$\bar{i}_{d1} = \frac{P_1}{V_{d1}} = P_1 = \frac{8N_1 V_{d2}}{\pi^2 N_2 \omega_s L_{12}} \sin \varphi_{12} + \frac{8N_1 V_{d3}}{\pi^2 N_3 \omega_s L_{13}} \sin \varphi_{13} \quad (7)$$

$$\bar{i}_{d2} = \frac{P_2}{V_{d2}} = -\frac{8N_1 V_{d1} \sin \varphi_{12}}{\pi^2 N_2 \omega_s L_{12}} + \frac{8N_1^2 V_{d3} \sin(\varphi_{13} - \varphi_{12})}{\pi^2 N_2 N_3 \omega_s L_{23}} \quad (8)$$

By applying partial differential operation in (7) and (8) respectively, (9) can be obtained for a steady-state operating point A ( $\varphi_{120}, \varphi_{130}$ ).

$$\begin{cases} G_{11} = \left. \frac{\partial \bar{i}_{d2}}{\partial \varphi_{12}} \right|_A = -\frac{8N_1 V_{d1} \cos \varphi_{120}}{\pi^2 N_2 N_3 \omega_s L_{12}} - \frac{8N_1^2 V_{d3} \cos(\varphi_{130} - \varphi_{120})}{\pi^2 N_2 N_3 \omega_s L_{23}} \\ G_{12} = \left. \frac{\partial \bar{i}_{d2}}{\partial \varphi_{13}} \right|_A = \frac{8N_1^2 V_{d3}}{\pi^2 N_2 N_3 \omega_s L_{23}} \cos(\varphi_{130} - \varphi_{120}) \\ G_{21} = \left. \frac{\partial \bar{i}_{d1}}{\partial \varphi_{12}} \right|_A = \frac{8N_1 V_{d2}}{\pi^2 N_2 \omega_s L_{12}} \cos \varphi_{120} \\ G_{22} = \left. \frac{\partial \bar{i}_{d1}}{\partial \varphi_{13}} \right|_A = \frac{8N_1 V_{d3}}{\pi^2 N_3 \omega_s L_{13}} \cos \varphi_{130} \end{cases} \quad (9)$$

Consequently, (9) can be simplified as (10).

$$\begin{bmatrix} \tilde{i}_{d2} \\ \tilde{i}_{d1} \end{bmatrix} = \begin{bmatrix} G_{11} & G_{12} \\ G_{21} & G_{22} \end{bmatrix} \begin{bmatrix} \tilde{\varphi}_{12} \\ \tilde{\varphi}_{13} \end{bmatrix} = \mathbf{G}_A \begin{bmatrix} \tilde{\varphi}_{12} \\ \tilde{\varphi}_{13} \end{bmatrix} \quad (10)$$

As shown in (9), besides the circuit parameters, the value of any matrix element in  $\mathbf{G}_A$ ,  $G_{xy}$  ( $x = 1, 2$  and  $y = 1, 2$ ) is determined by the steady-state parameters ( $\varphi_{120}$  and  $\varphi_{130}$ ). And it can be also seen from (10) that there are couplings between  $\tilde{i}_{d1}$  and  $\tilde{i}_{d2}$  caused by  $G_{21}$  and  $G_{12}$ .

The small signal linearization model of the three-port converter can be derived as in (11) by applying KCL and KVL laws in Figure 1.

$$\begin{cases} C_{d2} \frac{d\tilde{v}_{d2}}{dt} = -\frac{\tilde{v}_{d2}}{R_L} - G_{11} \tilde{\varphi}_{12} - G_{12} \tilde{\varphi}_{13} \\ L_{d1} \frac{d\tilde{i}_{ds}}{dt} = \tilde{v}_{d1} - \tilde{v}_{c1} - r_e \tilde{i}_{ds} \\ C_{d1} \frac{d\tilde{v}_{c1}}{dt} = \tilde{i}_{ds} - G_{21} \tilde{\varphi}_{12} - G_{22} \tilde{\varphi}_{13} \end{cases} \quad (11)$$

### 3. Control Strategy for TPC

#### 3.1. Decoupling Control for TPC

Assuming the matrix,  $\mathbf{G}_A$  given in (10) can be simplified to a diagonal matrix given in (12) by introducing a decoupling matrix  $\mathbf{H}$  defined in (13).

$$\begin{bmatrix} G_{11} & G_{12} \\ G_{21} & G_{22} \end{bmatrix} \begin{bmatrix} H_{11} & H_{12} \\ H_{21} & H_{22} \end{bmatrix} = \begin{bmatrix} G_{11} & 0 \\ 0 & G_{22} \end{bmatrix} \quad (12)$$

$$\mathbf{H} = \begin{bmatrix} H_{11} & H_{12} \\ H_{21} & H_{22} \end{bmatrix} = \begin{bmatrix} \frac{G_{11} G_{22}}{G_{11} G_{22} - G_{12} G_{21}} & \frac{-G_{12} G_{22}}{G_{11} G_{22} - G_{12} G_{21}} \\ \frac{-G_{11} G_{21}}{G_{11} G_{22} - G_{12} G_{21}} & \frac{G_{11} G_{22}}{G_{11} G_{22} - G_{12} G_{21}} \end{bmatrix} \quad (13)$$

The decoupling control block diagram is presented in Figure 2. In this figure,  $G_v$  and  $G_c$  represent the voltage controller and current controller respectively, which can be synthesized by using Bode plot based design method in frequency domain. In Figure 2, the open loop transfer functions of the voltage

and current control subsystems are  $G_{vo} = G_{11}G_1$  and  $G_{co} = G_{22}G_2$  respectively, the transfer functions of  $G_1$  and  $G_2$  are given in (14). The resonant angular frequency of  $G_2$  is  $\omega_n = 1/\sqrt{L_{d1}C_{d1}}$ .

$$\begin{cases} G_1(s) = \frac{R_L}{R_L C_{d2}s + 1} \\ G_2(s) = \frac{1}{L_{d1}C_{d1}s^2 + r_e C_{d1}s + 1} \end{cases} \quad (14)$$

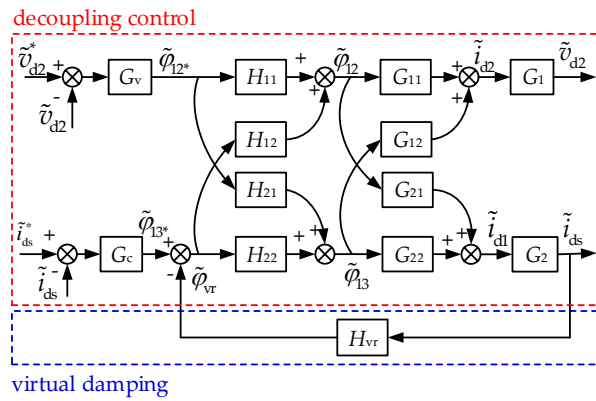


Figure 2. Decoupling control scheme of a three-port converter.

### 3.2. Virtual Damping Method

For Port 1 in Figure 1,  $L_{d1}$  and  $C_{d1}$  are utilized to constitute an LC filter to limit the amplitude of the double-switching frequency component of  $i_{ds}$  and reduce the negative impact of high-frequency ripple current on the power source (e.g., a fuel cell). However, this might cause performance degradation or an instability issue in current control subsystem due to the high resonant peak and a very weak damping ratio introduced by a pure LC circuit ( $r_e = 0$ ) or with a very small value of  $r_e$  shown in (14). Though the resonant phenomenon can be addressed by decreasing the current control bandwidth, the dynamic performance cannot be guaranteed.

The block diagram of the current control subsystem,  $G_{co} = G_{22}G_2$  is presented in Figure 3 according to (11). The transfer function,  $H_{vr}$  in Figure 2 is a compensation function that is proposed to implement virtual damping in this paper. The expression of  $H_{vr}$  is shown in Figure 3. In this figure,  $r_v$  is the desired virtual resistor. If the output of  $H_{vr}$ , which is  $\tilde{\varphi}_{vr}$ , is moved from the point A to the point B, then,  $H_{vr}$  in Figure 3 is changed to  $r_v/(s/\omega_p + 1)$ , and it makes  $H_{vr}$  a rational fraction.  $\omega_p$  is used to attenuate the high frequency noise, and if the value of  $\omega_p$  is high enough, then,  $r_v/(s/\omega_p + 1) \approx r_v$  becomes a resistor connected in series with  $r_e$ , and the damping ratio of  $G_2$  becomes  $(r_s + r_v)/2 \times \sqrt{C_{d1}/L_{d1}}$  with the introduction of  $r_v$  as a virtual resistor. In practical applications, the sampled  $i_{ds}$  is passed through  $H_{vr}$ , and then added to the output of the current controller to obtain the final phase shift between Port 1 and Port 3, and the value of  $\omega_p$  can be selected between  $\omega_s$  and  $\omega_s/2$ .

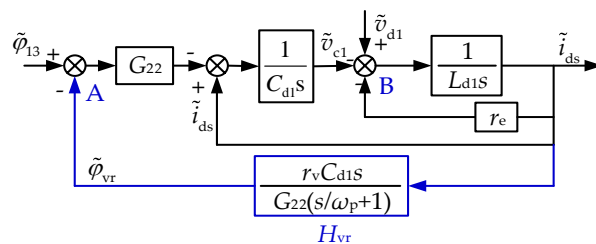


Figure 3. Schematic diagram of virtual damping implementation.

### 3.3. LADRC for TPC

The small signal model shown in (11) can be transformed into two subsystems to implement the LADRC based control method. The two differential equations for current control subsystem and voltage control subsystem are given by (15) and (16) respectively.

$$\ddot{\tilde{i}}_{ds} = -\frac{1}{C_{d1}L_{d1}}\tilde{i}_{ds} - \frac{r_e}{L_{d1}}\dot{\tilde{i}}_{ds} + \frac{G_{22}}{C_{d1}L_{d1}}\tilde{\varphi}_{12} + \frac{1}{L_{d1}}\dot{\tilde{v}}_{d1} + \left(\frac{G_{21}}{C_{d1}L_{d1}} - b_c\right)\tilde{\varphi}_{13} + b_c\tilde{\varphi}_{13} = f_c + b_c\tilde{\varphi}_{13} \quad (15)$$

$$\ddot{\tilde{v}}_{d2} = -\frac{1}{R_L C_{d2}}\tilde{v}_{d2} - \frac{G_{12}}{C_{d2}}\tilde{\varphi}_{13} + \left(-\frac{G_{11}}{C_{d2}} - b_v\right)\tilde{\varphi}_{12} + b_v\tilde{\varphi}_{12} = f_v + b_v\tilde{\varphi}_{12} \quad (16)$$

In (15) and (16),  $\tilde{v}_{d2}$  and  $\tilde{i}_{ds}$  are taken as the output variables of the two subsystems,  $\tilde{\varphi}_{13}$  and  $\tilde{\varphi}_{12}$  are the control signals of the current control subsystem and the voltage control subsystem respectively.

$\tilde{\varphi}_{13}$  is considered as an external disturbance of voltage control subsystem, while  $\tilde{\varphi}_{12}$  is considered as an external disturbance of the current control subsystem. Furthermore,  $f_c$  and  $f_v$  are used to represent the generalized disturbances that are associated with both inner and outer variable elements of the two subsystems (e.g., coupling, load, and operating point related parameter changes, etc.). In practical situations, the generalized disturbances,  $f_c$  and  $f_v$  are usually unknown and cannot be directly measured. Therefore, LESO is adopted to evaluate the generalized disturbances and relevant state variables in the LADRC method.

As for the current control subsystem,  $x_c = \left[\tilde{i}_{ds} \dot{\tilde{i}}_{ds} f_c\right]^T$  is selected as the state vector, the augmented state space model is formulated by (17)

$$\begin{cases} \dot{x}_c = A_c x_c + B_c \tilde{\varphi}_{13} + E_c f_c \\ \tilde{i}_{ds} = C_c x_c \end{cases} \quad (17)$$

where

$$\begin{cases} A_c = \begin{bmatrix} 0 & 1 & 0 \\ 0 & 0 & 1 \\ 0 & 0 & 0 \end{bmatrix} \\ B_c^T = \begin{bmatrix} 0 & b_c & 0 \end{bmatrix} \\ E_c^T = \begin{bmatrix} 0 & 0 & 1 \end{bmatrix} \\ C_c = \begin{bmatrix} 1 & 0 & 0 \end{bmatrix} \end{cases} \quad (18)$$

The LESO of current control subsystem is constructed by (19).

$$\begin{cases} \dot{z}_c = [A_c - L_c C_c]z_c + [B_c \quad L_c]w_c \\ y_c = z_c \end{cases} \quad (19)$$

where  $y_c = z_c = [z_{c1} \quad z_{c2} \quad z_{c3}]^T$  is the observed vector of  $x_c$ .  $w_c = [\tilde{\varphi}_{13} \quad \dot{\tilde{i}}_{ds}]^T$  and  $L_c$  given in (20) is the observer gain that can be designed using the pole placement method [17].

$$L_c = [3\omega_{oc} \quad 3\omega_{oc}^2 \quad \omega_{oc}^3]^T \quad (20)$$

where  $\omega_{oc}$  is the equivalent bandwidth of the observer.

It should be noted that the disturbance caused by the resonance of  $L_{d1}C_{d1}$  circuit is included in the generalized disturbance,  $f_c$ , therefore, the value of  $\omega_{oc}$  should be at least twice as large as  $\omega_n$ , that means  $\omega_{oc}/\omega_n \geq 2$  should be satisfied to make the LESO obtain accurate value of  $f_c$ , otherwise, the control performance might be significantly degraded.

Similarly, the LESO used for voltage control subsystem is presented in (21).

$$\begin{cases} \dot{z}_v = [A_v - L_v C_v]z_v + [B_v \quad L_v]w_v \\ y_v = z_v \end{cases} \quad (21)$$

In (21),  $w_v = [\tilde{\varphi}_{12} \quad \tilde{v}_{d2}]$ .  $y_v = z_v = [z_{v1} \quad z_{v2}]^T$  is the output vector of (21) that corresponds to  $x_v = [\tilde{v}_{d2} \quad f_v]^T$ . And the coefficient matrix in (21) are given in (22).

$$\begin{cases} A_v = \begin{bmatrix} 0 & 1 \\ 0 & 0 \end{bmatrix} \\ B_v^T = \begin{bmatrix} b_v & 0 \end{bmatrix} \\ E_v^T = \begin{bmatrix} 0 & 1 \end{bmatrix} \\ C_v = \begin{bmatrix} 1 & 0 \end{bmatrix} \end{cases} \quad (22)$$

The corresponding gain vector of the voltage LESO,  $L_v$  is shown in (23).

$$L_v = [2\omega_{ov} \quad \omega_{ov}^2]^T \quad (23)$$

Assuming  $f_c$  and  $f_v$  can be observed accurately ( $z_{c3} = f_c$ ,  $z_{v2} = f_v$ ), and if  $\tilde{\varphi}_{13}$  and  $\tilde{\varphi}_{12}$  in (15) and (16) can be expressed as (24).

$$\begin{cases} \tilde{\varphi}_{13} = \frac{(u_c - z_{c3})}{b_c} = \frac{(u_c - f_c)}{b_c} \\ \tilde{\varphi}_{12} = \frac{(u_v - z_{v2})}{b_v} = \frac{(u_v - f_v)}{b_v} \end{cases} \quad (24)$$

The current and voltage control subsystems will be simplified to two simple cascaded integrators systems shown in (25).

$$\begin{cases} \ddot{i}_{ds} = u_c \\ \dot{\tilde{v}}_{d2} = u_v \end{cases} \quad (25)$$

The current and voltage control signals,  $u_c$  and  $u_v$ , for this cascaded integrator system can be proposed as (26).

$$\begin{cases} u_c = k_{pc}(u_{rc} - z_{c1}) - k_{dc}z_{c2} \\ u_v = k_{pv}(u_{rv} - z_{v1}) \end{cases} \quad (26)$$

where  $k_{pc}$ ,  $k_{pv}$ , and  $k_{dc}$  are controller parameters, and  $u_{rc}$  and  $u_{rv}$  are current and voltage reference signals, respectively. In (26), it can be seen that  $u_c$  and  $u_v$  represent equivalent PD (proportional-derivative) and P (proportional) controllers respectively. The closed-loop transfer functions of the current and voltage control subsystem can be formulated as (27) and (28) which are obtained by substituting the two equations in (26) into the two equations of (25) respectively.

$$G_{cL} = \frac{k_{pc}}{s^2 + k_{dc}s + k_{pc}}, \quad (k_{pc} = \omega_c^2, k_{dc} = 2\xi\omega_c) \quad (27)$$

$$G_{vL} = \frac{k_{pv}}{s + k_{pv}}, \quad (k_{pv} = \omega_v) \quad (28)$$

In (27) and (28),  $\omega_c$  and  $\omega_v$  represent equivalent control bandwidths of the two closed-loop control subsystems with LADRC method, and  $\xi$  is the equivalent damping of the current control subsystem, which should be designed to guarantee smooth current change in transient state process (there is no intense oscillations in dynamic process). It can be seen from (27) and (28) that steady state errors are

eliminated in the current and voltage closed-loop control systems (when  $s = 0$ , unity gain is obtained in (27) and (28) respectively) by utilizing (26) as control law. Furthermore, the closed-loop control performances of the two subsystems are completely determined by the designed controller parameters ( $k_{pc}$ ,  $k_{pd}$  and  $k_{pv}$ ) regardless of the changes of model parameters. This is a prominent characteristic of the LADRC method.  $(\omega_c, \omega_{oc})$  and  $(\omega_v, \omega_{ov})$  are the adjustable LADRC parameters in current and voltage control subsystems, respectively. Since LADRC method is observer based, the bandwidth of the observer should be kept sufficiently larger than the bandwidth of the control system to realize effective compensation. Therefore, the two ratios,  $\alpha_c = \omega_{oc}/\omega_c$  and  $\alpha_v = \omega_{ov}/\omega_v$  should be larger than two at least in practical applications to get accurate observed values [21], otherwise, the control performance might not be guaranteed.

## 4. Simulation and Experimental Results

### 4.1. Simulation Results

In order to verify the theoretical analysis and design results of the proposed method, a simulation model of the isolated TPC is developed by using MATLAB/Simulink, and the main parameters of the simulation model are listed in Table 1.

**Table 1.** Parameters of The Simulation Model.

Symbol	Name	Value
$v_{d1}$	DC input voltage	24 V
$v_{d2}$	Output voltage	36 V
$v_{d3}$	Battery voltage	24 V
$L_{d1}$	Input filter inductor	100 $\mu$ H
$r_e$	Input filter inductor ESR	0.1 $\Omega$
$C_{d1}$	Input filter capacitor	1200 $\mu$ F
$C_{d2}$	Output filter capacitor	1000 $\mu$ F
$R_L$	Load resistor	45 $\Omega$ /22 $\Omega$
$f_s$	Switching frequency	20 kHz

The steady-state operating point A (0.620, 0.379) is selected which corresponds to  $R_L = 45 \Omega$ ,  $v_{d2} = 36$  V and  $i_{ds} = 1.3$  A, and an extra 0.2  $\Omega$  virtual resistor is introduced. The open loop transfer functions of the two subsystems are obtained by substituting the parameters listed in Table 1 into  $G_{co}$  and  $G_{vo}$ , respectively. The controllers  $G_c$  and  $G_v$ , given by (29), are designed for the decoupled current and voltage subsystems respectively by using the frequency domain design method.

$$\begin{cases} G_c = \frac{500}{1 \times 10^{-4}s^2 + s} \\ G_v = \frac{0.2813s + 6.25}{1 \times 10^{-8}s^3 + 2 \times 10^{-4}s^2 + s} \end{cases} \quad (29)$$

The Bode plots of the two subsystems with and without correction are shown in Figures 4a and 4b, respectively.

As can be seen in Figure 4a, the crossover frequency of the corrected current control subsystem with  $r_v = 0.2$  (the curve B) is about 71 Hz, the phase margin is about  $81^\circ$ , and the gain margin is about 7 dB. The crossover frequency of the corrected voltage control subsystem is about 75 Hz, the phase margin is about  $85^\circ$ , and the gain margin is about 33 dB. As a comparison, if  $r_v = 0.2$  is cancelled, the corrected current control subsystem (the curve C) will be unstable, since the resonant peak (the corresponding angular frequency is  $\omega_n = 2887$  rad/s) of the curve C will intersect with 0 dB axis under this condition.

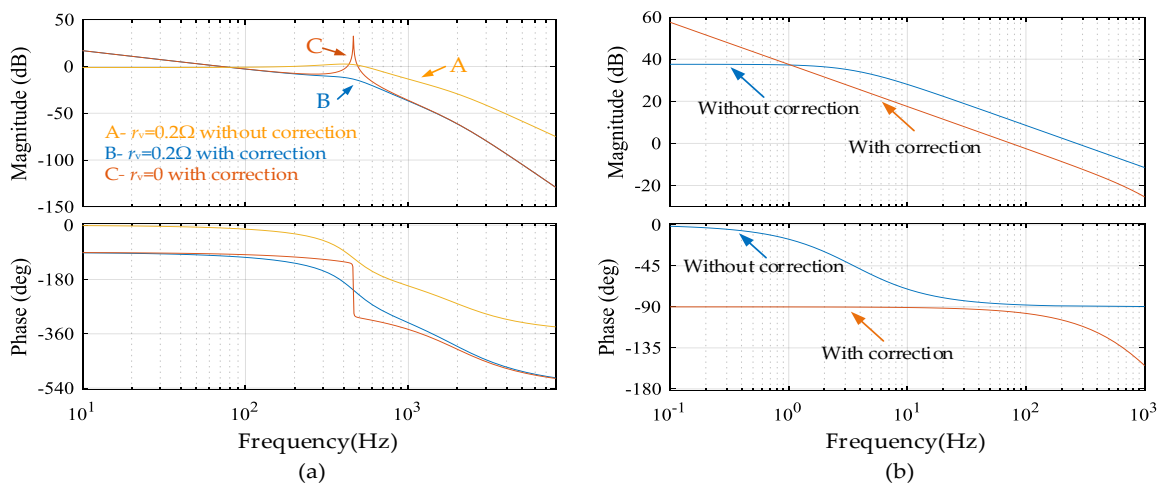


**Figure 4.** The bode plots of subsystems by using traditional frequency control method: (a)  $i_{ds}$  subsystem; (b)  $v_{d2}$  subsystem.

For the control systems with LADRC method, the equivalent control bandwidths of the current and voltage subsystems are the same,  $\omega_c = \omega_v = 450$  rad/s (about 72 Hz) which are close to the designed crossover frequencies using the traditional frequency domain method. The observer bandwidths of the current and voltage subsystems are  $\omega_{oc} = 4147$  rad/s (about 660 Hz), and  $\omega_{ov} = 2000$  rad/s (about 318 Hz) respectively. The simulation results are shown in Figure 5.

Figure 5a shows simulation results of  $v_{d2}$  and  $i_{ds}$  with traditional frequency control under a step load change condition. As can be seen in Figure 5a, there is an obvious voltage drop (from 36 V to 35.2 V) at 0.5 s when the load is suddenly changed from 29 W to 52 W that resulted in transient fluctuations in  $i_{ds}$  (changed from 1.3 A to 1.25 A). When the load is suddenly reduced at 0.7s from 52 W to 29 W, current  $i_{ds}$  transiently increases from 1.3 A to 1.37 A, while  $v_{d2}$  increases to about 36.8 V, and then decreases gradually to its rated value after 100 ms.

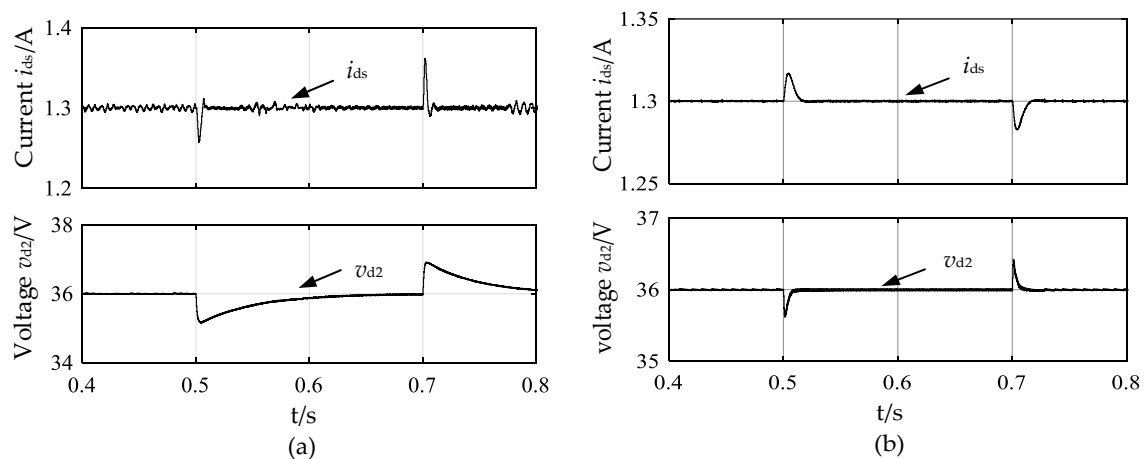


**Figure 5.** The simulation results of the system: (a) with traditional frequency control method; (b) with the LADRC method.

The simulation results of the system with the LADRC method and  $r_v = 0.2 \Omega$  are shown in Figure 5b. In this figure, it can be seen that for the same load change,  $v_{d2}$  drops from 36 V to 35.6 V at 0.5 s when the load increased, and it increases from 36 V to 36.4 V at 0.7 s when the load decreases. However, current is changed slightly with respect to the load change. For instance, the current drops from 1.3 A to 1.28 A when the load reduced and it increases from 1.3 A to 1.32 A when the load is increased. By comparing the result shown in Figure 5, it can be seen that the amplitude of  $i_{ds}$

fluctuation in the system controlled with LADRC is lower than that of the system controlled with the traditional frequency control method. Also, the transient recovery time of  $v_{d2}$  is much shorter than that of the system with the traditional frequency control. These results imply that the information of the load change observed by LESO is effectively utilized in the control system.

#### 4.2. Experimental Validation and Analysis

In order to further verify the effectiveness of the proposed method, an experimental platform was developed as shown in Figure 6. The circuit parameters and load change conditions of the experimental system are similar to the simulation model. The experimental results are shown in Figures 7–11.

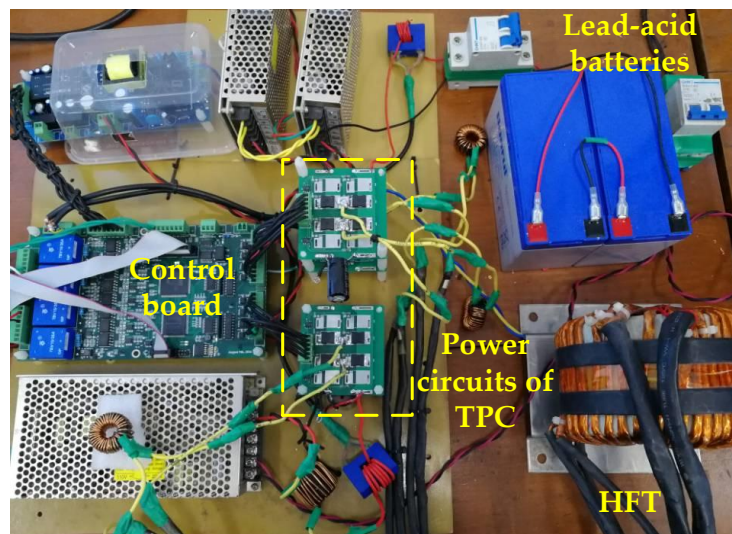


Figure 6. Hardware experiment circuit of the three-port converter.

Figure 7 shows the experimental results,  $i_{ds}$ ,  $v_{d2}$ ,  $\Delta v_{d2}$  (fluctuation of  $v_{d2}$ ) and  $i_o$  achieved for the developed converter controlled with the traditional frequency control method. The results of  $i_{ds}$  and  $\Delta v_{d2}$  ( $v_{d2}$  was controlled to 36 V) for a sudden load increase are shown in Figure 7a. As shown in this figure, there is about 0.24 A drop in  $i_{ds}$  and 0.8 V drop in  $v_{d2}$  when the load is suddenly changed from 29 W to 52 W. Figure 7b shows the current and voltage changes with respect to sudden load drop where the current and voltage are increased by about 0.24 A and 0.9 V respectively.

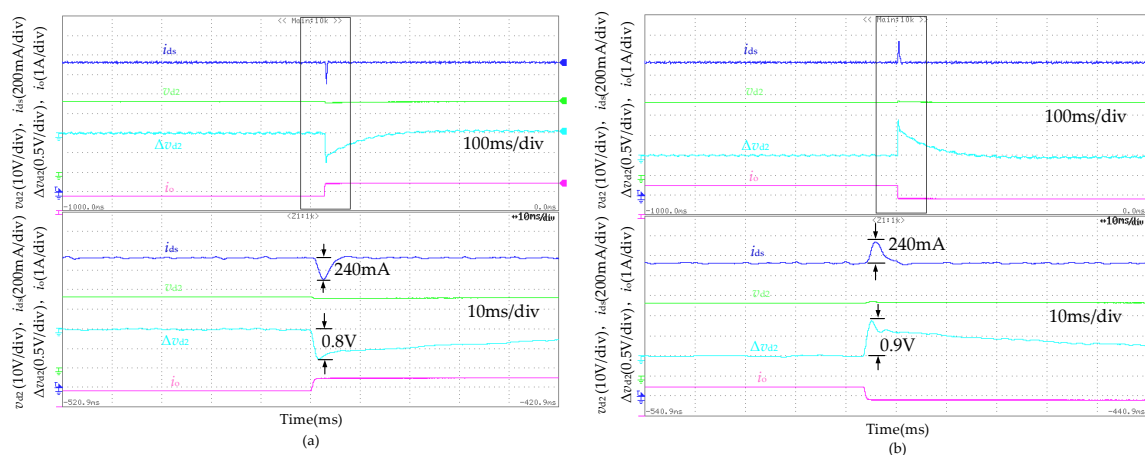
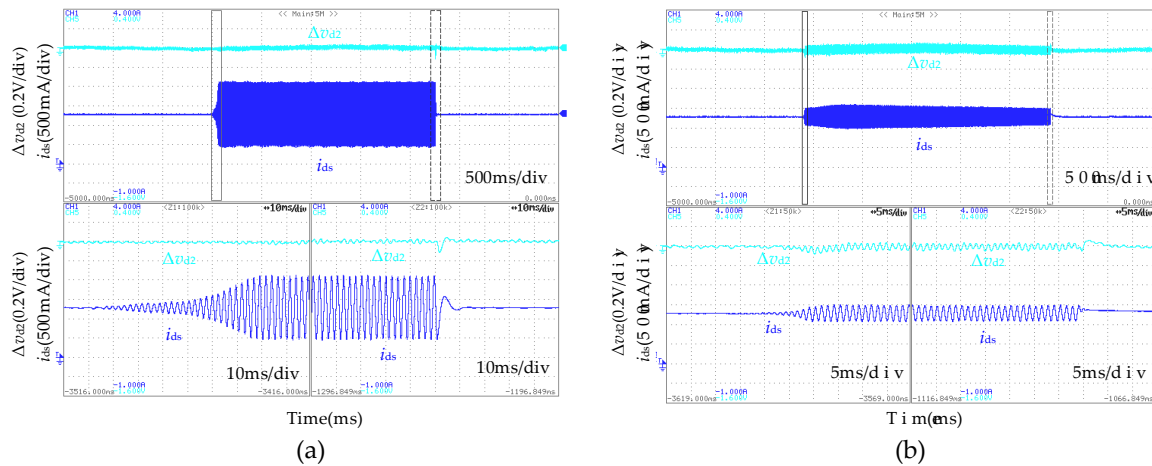


Figure 7. The experiment results of  $i_{ds}$ ,  $v_{d2}$ ,  $\Delta v_{d2}$  and  $i_o$  with the traditional frequency control method and  $r_v = 0.2 \Omega$ : (a) sudden load increase; (b) sudden load decrease.

The effect of the proposed virtual resistor method on  $i_{ds}$  control is conducted by removing and re-adding the virtual resistor with the same current controller used in Figure 7. The experimental results are shown in Figure 8a, it can be seen that there are serious oscillations in  $i_{ds}$  (the current control subsystem is unstable in this case as indicated by the curve C in Figure 4 and voltage ripples ( $\Delta v_{d2}$ ) of  $v_{d2}$  are also increased with the same oscillation frequency of  $i_{ds}$ . While the virtual resistor scheme is re-performed, the oscillation of  $i_{ds}$  can be suppressed soon, and the amplitude of voltage ripple in  $v_{d2}$  becomes lower.



**Figure 8.** The experimental results with and without  $r_v = 0.2 \Omega$  virtual resistor ( $\omega_n = 2887 \text{ rad/s}$ ): (a) traditional frequency control; (b) LADRC.

The experimental results of  $i_{ds}$ ,  $v_{d2}$ ,  $\Delta v_{d2}$  and  $i_o$  with the LADRC method and  $r_v = 0.2 \Omega$  are shown in Figure 9. As shown in Figure 9a, when the same load increment (23 W) is experienced small changes are observed in  $i_{ds}$  (changes from 1.3 A to 1.35 A) and  $v_{d2}$  (changes from 36 V to 35.6 V) because of the coupling between current and voltage subsystems. As shown in Figure 9b, for a sudden load reduction,  $i_{ds}$  is changed from 1.3 A to 1.25 A, and  $v_{d2}$  is increased for about 0.5 V. Also, as illustrated in Figure 9, the fluctuations of  $i_{ds}$  and  $v_{d2}$  in the transient process with the LADRC method are lower than those with the traditional frequency control method as shown in Figure 7, and the voltage transient recovery time with the LADRC method is much shorter than that with the traditional frequency control. These results indicate that the control system with the LADRC has better decoupling performance and adaptability to the operating point changes compared to the control system with the traditional frequency control.

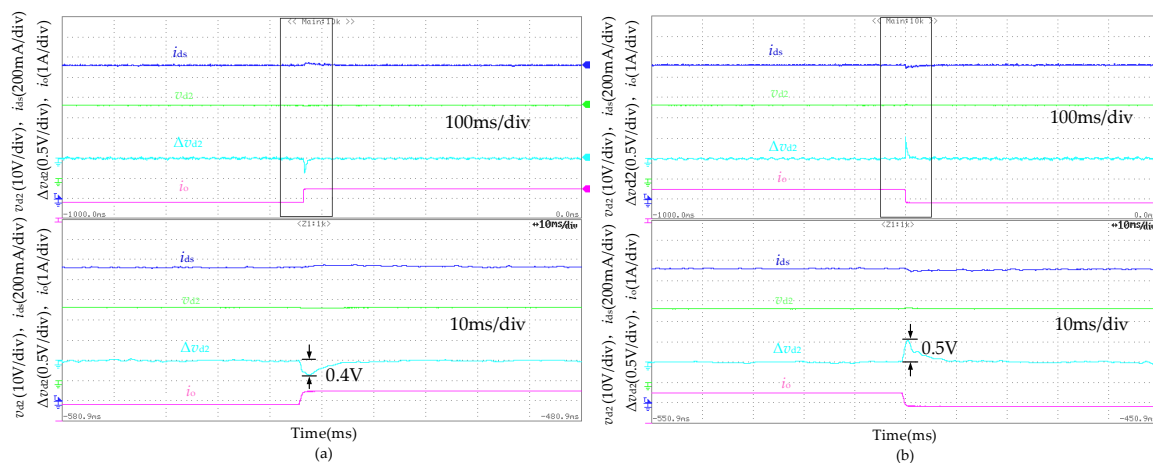


**Figure 9.** The experimental results of  $i_{ds}$ ,  $v_{d2}$ ,  $\Delta v_{d2}$  and  $i_o$  with LADRC method,  $\omega_n = 2887 \text{ rad/s}$  and  $r_v = 0.2 \Omega$ : (a) sudden load increase; (b) sudden load decrease.

The experimental result with and without  $0.2 \Omega$  virtual resistor with LADRC method and  $\omega_n = 2887 \text{ rad/s}$  is presented in Figure 8b. As shown in this figure, there are obvious current oscillations in  $i_{ds}$  when  $r_v = 0.2 \Omega$  is removed, since the observer bandwidth ( $\omega_{oc} = 4147 \text{ rad/s}$ ) is not sufficiently higher than the resonant angular frequency of  $L_{d1}C_{d1}$  circuit ( $\omega_{oc}/\omega_n \approx 1.43 < 2$ ). And it is similar to the case shown in Figure 8a, the current oscillations can be attenuated effectively if the virtual resistor method is reused.

For comparison study, the resonant angular frequency of  $G_2(s)$  in (14) is reduced to  $\omega_n = 1521 \text{ rad/s}$  (by setting  $L_{d1} = 160 \mu\text{H}$  and  $C_{d1} = 2700 \mu\text{F}$ ), then there is no oscillations in  $i_{ds}$  as shown in Figure 10, that means  $i_{ds}$  can be controlled well since the ratio of  $\omega_{oc}/\omega_n$  is about 2.73 which is larger than two in this case, it means that the impact caused by the resonance of  $L_{d1}C_{d1}$  circuit can be much accurately observed by the LESO.

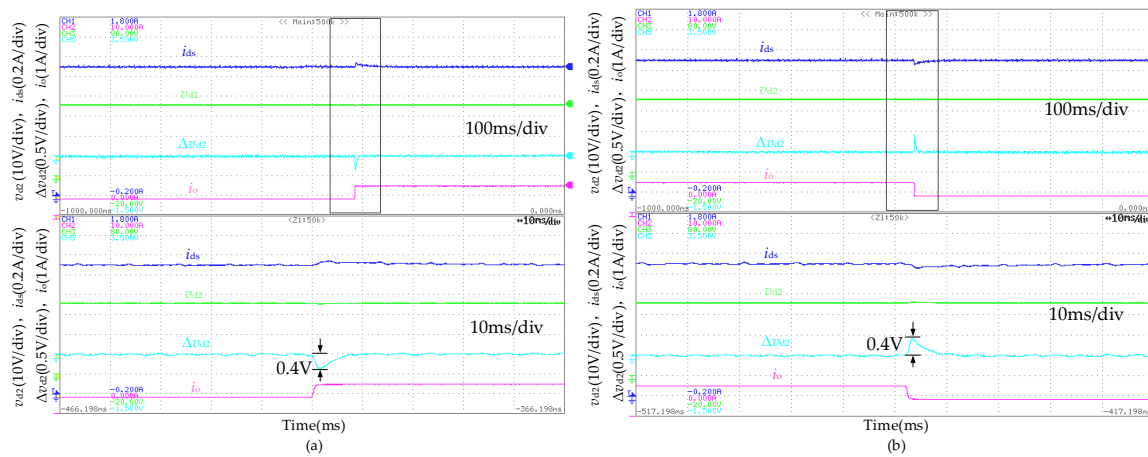


**Figure 10.** The experimental results of  $i_{ds}$ ,  $v_{d2}$ ,  $\Delta v_{d2}$  and  $i_o$  with LADRC method,  $\omega_n = 1521 \text{ rad/s}$  and  $r_v = 0 \Omega$ : (a) sudden load increase; (b) sudden load decrease.

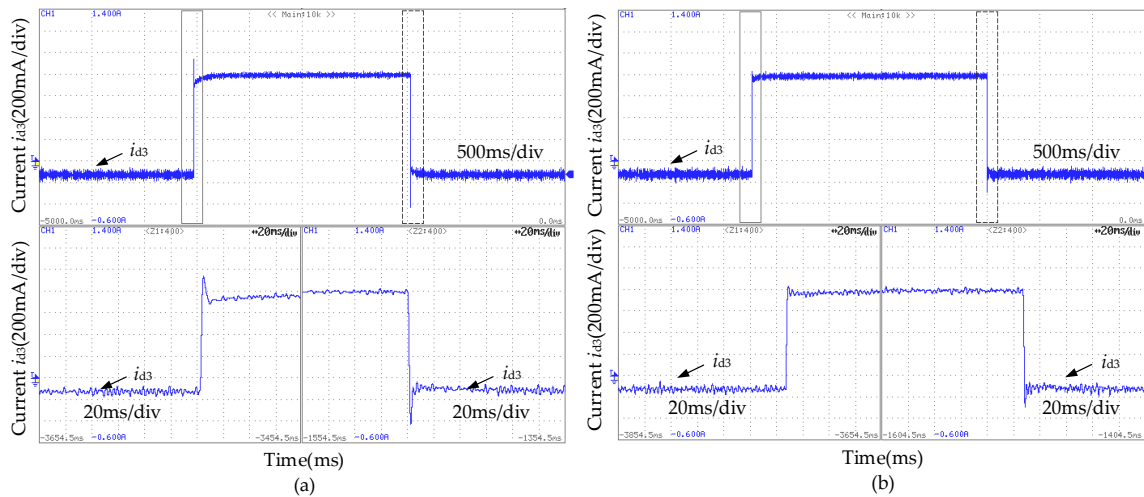


**Figure 11.** The experimental results of battery current  $i_{d3}$ : (a) traditional frequency control; (b) LADRC.

The battery current  $i_{d3}$  for the traditional frequency control and LADRC are shown in Figures 11a and 11b, respectively. In Figure 11, it can be seen that not only the overshoot of  $i_{d3}$  with the LADRC is relatively lower, but also the transient recovery time of  $i_{d3}$  is shorter than that obtained using the traditional frequency control. This indicates the LADRC method can provide better dynamic balance in the power delivery process. The results shown in Figure 11 have some internal relations with the experimental results presented in Figures 7 and 9. For instance, compared to Figure 11b with LADRC

method applied, the battery overshoot current,  $i_{d3}$  shown in Figure 11a is larger when traditional frequency control method is applied. Larger overshoot current causes significant drop in  $i_{ds}$  shown in Figure 7a, whereas smaller overshoot of  $i_{d3}$  shown in Figure 11b with LADRC resulted in much smaller overshoot in  $i_{ds}$  shown in Figure 9a.

## 5. Conclusions

The model parameter variation caused by the operating point changes and couplings between different ports during power delivery in an isolated three-port converter has a negative impact on the converter control performance. In this study, the LADRC method is employed to control the three-port converter. In the LADRC method, the possible model parameter uncertainties, load changes and the negative impact of LC circuit resonance are all expressed as a generalized disturbance that is considered as a state variable and observed by the LESO which is utilized to synthesize the control signal. In this method, the bandwidth of the LESO is sufficiently higher than the equivalent control bandwidth and the resonant frequency of LC circuit that guarantee the system dynamics and generalized disturbance can be accurately observed. Therefore, the desired closed-loop control performance that is independent of parameters changes and external disturbances can be obtained. And a virtual resistor based method is proposed to increase damping ratio of the current control subsystem of TPC which is beneficial to further improve current control performance using LADRC method. The simulation and experimental results revealed that the proposed method is robust against model parameter changes and external disturbances. Therefore, the dynamic control performance of the three-port converter can be improved significantly.

**Author Contributions:** Conceptualization, J.Y., M.L. and H.C.; Validation, M.L., J.Y. and H.C.; Writing-Original Draft Preparation, J.Y. and H.C.; Writing-Review & Editing, N.G., M.V. and M.L.

**Funding:** This work is sponsored by the National Natural Science Foundation of China (No.51479042 and No. 51761135013), and the fundamental research funds for the central universities of China (No. HEUCFG201822).

**Conflicts of Interest:** The authors declare no conflict of interest.

## References

1. Tao, H.; Kotsopoulos, A.; Duarte, J.L.; Hendrix, M.A.M. Design of a soft-switched three-port converter with DSP control for power flow management in hybrid fuel cell systems. In Proceedings of the 2005 European Conference on Power Electronics and Applications, Dresden, Germany, 11–14 September 2005.
2. Tao, H.; Duarte, J.L.; Hendrix, M.A.M. A Distributed Fuel Cell Based Generation and Compensation System to Improve Power Quality. In Proceedings of the 2006 CES/IEEE 5th International Power Electronics and Motion Control Conference, Shanghai, China, 14–16 August 2006.
3. Ling, Z.; Wang, H.; Yan, K.; Sun, Z. A new three-port bidirectional DC/DC converter for hybrid energy storage. In Proceedings of the 2015 IEEE 2nd International Future Energy Electronics Conference (IFEEEC), Taipei, Taiwan, 1–4 November 2015.
4. Tao, H.; Duarte, J.L.; Hendrix, M.A.M. Line-Interactive UPS Using a Fuel Cell as the Primary Source. *IEEE Trans. Ind. Electron.* **2008**, *55*, 3012–3021. [[CrossRef](#)]
5. Wang, L.; Wang, Z.; Li, H. Optimized energy storage system design for a fuel cell vehicle using a novel phase shift and duty cycle control. In Proceedings of the 2009 IEEE Energy Conversion Congress and Exposition, San Jose, CA, USA, 20–24 September 2009.
6. Kim, S.Y.; Song, H.S.; Nam, K. Idling Port Isolation Control of Three-Port Bidirectional Converter for EVs. *IEEE Trans. Power Electron.* **2012**, *27*, 2495–2506. [[CrossRef](#)]
7. Jiang, Y.; Liu, F.; Ruan, X.; Wang, L. Optimal idling control strategy for three-port full-bridge converter. In Proceedings of the 2014 International Power Electronics Conference (IPEC-Hiroshima 2014—ECCE ASIA), Hiroshima, Japan, 18–21 May 2014.
8. Ajami, A.; Asadi Shayan, P. Soft switching method for multiport DC/DC converters applicable in grid connected clean energy sources. *IET Power Electron.* **2015**, *8*, 1246–1254. [[CrossRef](#)]

9. Tao, H.; Duarte, J.L.; Hendrix, M.A.M. Three-Port Triple-Half-Bridge Bidirectional Converter with Zero-Voltage Switching. *IEEE Trans. Power Electron.* **2008**, *23*, 782–792. [[CrossRef](#)]
10. Tao, H.; Kotsopoulos, A.; Duarte, J.L.; Hendrix, M.A.M. A Soft-Switched Three-Port Bidirectional Converter for Fuel Cell and Supercapacitor Applications. In Proceedings of the 2005 IEEE 36th Power Electronics Specialists Conference, Recife, Brazil, 12 June 2005.
11. Zhao, C.; Kolar, J.W. A novel three-phase three-port UPS employing a single high-frequency isolation transformer. In Proceedings of the 2004 IEEE 35th Annual Power Electronics Specialists Conference, Aachen, Germany, 20–25 June 2004.
12. Zhao, C.; Round, S.D.; Kolar, J.W. An Isolated Three-Port Bidirectional DC-DC Converter with Decoupled Power Flow Management. *IEEE Trans. Power Electron.* **2008**, *23*, 2443–2453. [[CrossRef](#)]
13. Tao, H.; Kotsopoulos, A.; Duarte, J.L.; Hendrix, M.A.M. Transformer-Coupled Multiport ZVS Bidirectional DC-DC Converter with Wide Input Range. *IEEE Trans. Power Electron.* **2008**, *23*, 771–781. [[CrossRef](#)]
14. Wang, L.; Wang, Z.; Li, H. Asymmetrical Duty Cycle Control and Decoupled Power Flow Design of a Three-port Bidirectional DC-DC Converter for Fuel Cell Vehicle Application. *IEEE Trans. Power Electron.* **2012**, *27*, 891–904. [[CrossRef](#)]
15. Falcones, S.; Ayyanar, R. LQR control of a quad-active-bridge converter for renewable integration. In Proceedings of the 2016 IEEE Ecuador Technical Chapters Meeting (ETCM), Guayaquil, Ecuador, 12–14 October 2016.
16. Gao, Z. Active disturbance rejection control: From an enduring idea to an emerging technology. In Proceedings of the 2015 10th International Workshop on Robot Motion and Control (RoMoCo), Poznan, Poland, 24 August 2015.
17. Gao, Z. Scaling and bandwidth-parameterization based controller tuning. In Proceedings of the 2003 American Control Conference, Denver, CO, USA, 4–6 June 2003.
18. Wang, W.; Gao, Z. A comparison study of advanced state observer design techniques. In Proceedings of the 2003 American Control Conference, Denver, CO, USA, 4–6 June 2003.
19. Miklosovic, R.; Radke, A.; Gao, Z. Discrete implementation and generalization of the extended state observer. In Proceedings of the 2006 American Control Conference, Minneapolis, MN, USA, 14–16 June 2006.
20. Sun, B.; Gao, Z. A DSP-based active disturbance rejection control design for a 1-kW H-bridge DC-DC power converter. *IEEE Trans. Ind. Electron.* **2005**, *52*, 1271–1277. [[CrossRef](#)]
21. Zhu, B. *Introduction of Active Disturbance Rejection Control*, 1st ed.; Beihang University Press: Beijing, China, 2017; pp. 42–45.



© 2018 by the authors. Licensee MDPI, Basel, Switzerland. This article is an open access article distributed under the terms and conditions of the Creative Commons Attribution (CC BY) license (<http://creativecommons.org/licenses/by/4.0/>).